

CCD Photometric Precision for the Transiting Exoplanet  
Survey Satellite (TESS)

by

Lulu Liu

SUBMITTED TO THE DEPARTMENT OF PHYSICS IN PARTIAL  
FULFILLMENT OF THE REQUIREMENTS FOR THE DEGREE OF

BACHELOR OF SCIENCE IN PHYSICS  
AT THE  
MASSACHUSETTS INSTITUTE OF TECHNOLOGY  
[JUNE]  
MAY 2009

**ARCHIVES**

© 2009 Lulu Liu. All rights reserved.

The author hereby grants to MIT permission to reproduce  
and to distribute publicly paper and electronic  
copies of this thesis document in whole or in part  
in any medium now known or hereafter created.

Signature of Author: \_\_\_\_\_

\_\_\_\_\_  
Department of Physics

May 21, 2009

Certified by: \_\_\_\_\_

\_\_\_\_\_  
George R. Ricker

Senior Research Scientist - P.I. of TESS Mission

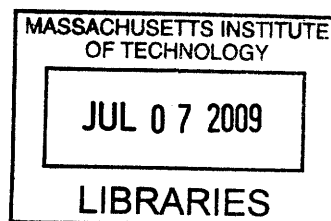
Thesis Supervisor

Accepted by: \_\_\_\_\_

\_\_\_\_\_  
David E. Pritchard

Professor of Physics

Senior Thesis Coordinator



# CCD Photometric Precision for the Transiting Exoplanet Survey Satellite (TESS)

Lulu Liu

Submitted to the Department of Physics on May 21, 2009 in Partial  
Fulfillment of the Requirements for the degree of Bachelor of Science  
in Physics

## **Abstract**

We seek to fully characterize all noise contributions along the CCD and electronics signal path specific to the equipment to be used on board the TESS all-sky space observatory. We adjust physical variables in such a way as to minimize this noise and achieve a photometric precision limited in large part by shot noise. Ultimately, the goal is to demonstrate in the lab, by analyzing photon data generated by LED simulated stars and using relative photometric techniques, that TESS CCDs and electronics are capable of performing photometry at the 100ppm (parts per million) level as required by the goals of the space mission. In our investigation, we are limited by unusually high readout noise in the CCD electronics but still able to achieve reliable sub-200ppm level photometry in the lab.

# Contents

<b>1</b>	<b>Background in Transiting Exoplanet Science</b>	<b>3</b>
<b>2</b>	<b>Introduction</b>	<b>4</b>
<b>3</b>	<b>Breakdown of Major Noise Sources</b>	
	<b>Limiting Photometry</b>	<b>5</b>
3.1	Shot Noise . . . . .	5
3.2	Dark Current . . . . .	5
3.3	Variations in Quantum Efficiency . . . . .	6
3.4	Saturation and Pixel Overflow . . . . .	7
3.5	Readout Noise . . . . .	7
3.6	Gain and A/D Converter Nonlinearity . . . . .	8
3.7	Error Propagation Formula . . . . .	9
<b>4</b>	<b>Means and Methods</b>	<b>9</b>
4.1	Data-Taking Strategy . . . . .	9
4.1.1	Equipment and Set-up . . . . .	9
4.1.2	Temperature Control . . . . .	10
4.1.3	Dark Current Elimination . . . . .	11
4.1.4	Strategy for Dealing with Pixel-to-Pixel Variation . . . . .	13
4.1.5	Humidity's Effect on Photometry . . . . .	14
4.1.6	Stability of LED Light Source . . . . .	14
4.1.7	Undersaturating Pixels and A/D Bits . . . . .	16
4.2	Analysis Strategy . . . . .	16
4.2.1	Image Stacking and Stamp-Size Subarrays . . . . .	16
4.2.2	Background/Bias Subtraction . . . . .	17
4.2.3	Star Field Intensity Profile and Relative Photometry . . . . .	19
4.3	Summary . . . . .	22
<b>5</b>	<b>Calibration - CCD Gain</b>	<b>22</b>
5.1	Relation to Shot Noise of a Bright Source . . . . .	23
5.2	Calibrating to X-Ray Photons of Known Energy . . . . .	24
<b>6</b>	<b>Photometry</b>	<b>27</b>
6.1	Star Plate Layout and Star Reference Numbers . . . . .	27

6.2	Signal to Noise as a Function of Bounding Radius . . . . .	28
6.3	Intensity Correlations with Temperature and Position . . . . .	29
6.4	Light Curves . . . . .	33
6.4.1	Shot Noise Limit? . . . . .	33
6.4.2	Exclusions . . . . .	33
6.4.3	Photometry Results . . . . .	34
6.4.4	Analysis . . . . .	36
<b>7</b>	<b>Conclusions and the Future</b>	<b>39</b>
<b>8</b>	<b>Acknowledgements</b>	<b>40</b>

# 1 Background in Transiting Exoplanet Science

The first confirmed discovery of an extrasolar planet (or exoplanet) around a Sun-like star occurred in 1995 to the fascination of scientists and non-scientists alike , [9] (Mayor & Queloz, 1995). Not only did the announcement touch off a new era in the human ongoing search for company in the universe, it also launched a now very exciting subfield of astronomy and astrophysics devoted to the discovery and study of these bodies. Since 1995, hundreds of exoplanets have been discovered orbiting main-sequence stars, with the rate of discovery increasing each year. The vast majority of these planets were detected through radial velocity measurements of its host star. Now, improved instrumentation has allowed us new observational techniques. The result? Along with the advantage of more frequent discoveries, new additions to the exoplanet database now show an increased diversity, and greater detailed knowledge has been gained about planets new and old. One recently expanded observational technique takes advantage of a somewhat rare occurrence: transits.

Transiting extrasolar planets are a special class of exoplanets distinguished by a property of their orbits which allows for a particularly simple method of detection. A transiting exoplanet is one which periodically “transits” or passes through our line of sight to the host star, blocking some otherwise incident light and reducing the measured brightness of the star. Close to the star, about 10% of planets exhibit transits, but this probability decreases with both increasing radius of orbit and decreasing star size [13] (Ricker, *et al*). The physics of transiting exoplanet discovery then centers around detecting these very small, periodic changes in the intensity of radiation from a star as to indirectly determine the presence of an orbiting body, and such a search generally monitors many stars all at once.

Ground-based surveys have contributed to the discovery of about 20 exoplanets using this technique, but are limited in sensitivity by “red noise”, or noise associated with the deflection and absorption of star light by the atmosphere, to about 1%, or 10,000 ppm (parts per million) [12] (Pont, *et al*, 2007). Transits associated with smaller planets, with depths of less than 10,000 ppm, are lost in this noise floor, so ground-based searches strongly favor “hot Jupiters”, or large planets orbiting very close to its bright, parent star. A whole new level of photometry can be achieved in space. A survey conducted in low-Earth orbit can neglect to great approximation any atmospheric effects and conduct photometry at the level limited only by shot noise from the source and CCD and electronics noise from the instrument itself. The

improved sensitivity allows us to dip into the regime of earth-like planets: planets with radii several times the radius of Earth orbiting in more habitable regions. The Transiting Exoplanet Survey Satellite (TESS), set for launch in 2012, hopes to avail itself of its location in space to directly observe the transits of approximately 1000 so far undiscovered exoplanets, greatly expanding the current database. Particularly significant is its target of nearby, bright stars for candidate exoplanets, which bodes well for subsequent ground-based followup verification and determination of other important properties such as mass, composition, existence of an atmosphere, presence of water, and so on.

## 2 Introduction

TESS is poised at this moment to make promising contributions to the field of exoplanet science. However, its ultimate success in yielding the desired number and range of extrasolar planets rests in the photometric precision of its onboard equipment. From the initial release of a photon by the parent star to the final electrical signal output that constitutes a measurement of this photon, the signal path, even assuming vacuum space, is fraught with noise. The inescapable photon shot noise aside, the bulk of the noise resides in the CCD itself, from the effects of pixel-to-pixel variation, charge transfer errors, dark current, saturation and pixel overflow, charge diffusion, and so on. The rest is added by the electronics during the conversion from electron signal to digital “counts”, also known as ADUs, or analog-to-digital units. Two effects are most notable during this signal transfer: the addition on a per pixel basis of a random readout noise, and a systematic effect called integral nonlinearity, which is most significantly observed for CCD pixels near saturation. Each additional noise parameter accordingly decreases the photometric precision of the observing instrument as a whole and contributes to its departure from shot-noise limited photometry.

The subsequent investigation detailed in this paper is, at its core, a full-scale characterization and quantification of all significant contributions of noise along the signal path. As a secondary objective, we will demonstrate, in the lab, using simulated stars and flight-ready CCDs and electronics, 100 ppm photometry, as required by the current mission model for the Transiting Exoplanet Survey Satellite.

## 3 Breakdown of Major Noise Sources

### Limiting Photometry

#### 3.1 Shot Noise

Any Poisson process, or stochastic process characterized by continuous and independent events occurring at a constant average rate, obeys Poisson statistics which states that the measured rate of occurrence of these events for any given interval of time,  $k$ , can be described by the probability mass function, which also depends on the average rate,  $N$ ,

$$p(k, N) = \frac{N^k e^{-N}}{k!} \quad (1)$$

Here,  $N$  is both the mean and variance of the distribution in units of counts per time. The generation of photons by stellar and electrical processes obeys Poisson statistics and therefore so does the rate of arrival of these photons at each individual CCD pixel. In the limit of large  $N$ , the Poisson distribution approaches a normal (Gaussian) distribution with a standard deviation of  $\sqrt{N}$ . This inherent noise which accompanies any signal generated by a Poisson process is termed “shot noise”. The signal-to-noise ratio (SNR) due to shot noise alone is given by,

$$SNR = S/N = N/\sqrt{N} = \sqrt{N} \quad (2)$$

which goes up as the signal increases in power.

#### 3.2 Dark Current

For a system in thermal equilibrium at temperature  $T$ , the probability that any particle in this system is in a state with energy  $E$  is proportional to the Boltzmann factor,  $e^{-\frac{E}{kT}}$ , with  $k$  representing the Boltzmann constant. From this relationship, we can see that any system at a temperature greater than absolute zero will necessarily encounter thermal excitation and associated thermal noise. This is true of CCDs as well. CCD signals are generated by the excitation of electrons from the valence band of the semiconductor detector material into the conduction band. These electrons are collected in potential wells (pixels) and then transferred out of the active region of the CCD to be read out as current. Thermal excitation can result in positive signals which are indistinguishable from that produced by actual photons. This false signal is what is referred to as “dark current”.

The amount of dark current in a CCD device is a strong function of its temperature. As temperature increases, available energy increases, and dark current goes up. The band gap of the absorbing material also plays a role. The band gap energy,  $E_g$ , is the minimum energy needed to promote a valence band electron into the conduction band. The greater the band gap, the lower the resolution per pixel, the less dark current at a given temperature. Equation 3 gives the general empirical expression for average dark current, in units of electrons per pixel per second, as a function of temperature and band gap energy [1](Bely, 2003).

$$N_{dc} \propto T^{\frac{3}{2}} e^{-\left(\frac{E_g}{2kT}\right)} \quad (3)$$

Because dark current generation is also a Poisson process, on a per pixel basis, deviations from average follow shot noise statistics. That is,

$$\sigma_{dc} = \sqrt{N_{dc}} \quad (4)$$

Dark current can also contribute non-uniformly from pixel to pixel, resulting in CCD structure, or systematic noise.

### 3.3 Variations in Quantum Efficiency

No device is 100% efficient. For a certain number of photons incident upon a detector, some of them will be absorbed, a number will be reflected, and the rest will pass right through the device. The quantum efficiency of a device is simply the ratio between the number of photons absorbed (and accounted for) and the number of incident photons, usually given on a percent basis. It is sensitive to changes in the thickness of the absorbing semiconductor material, various coatings applied to the surface of the CCD, temperature, wavelength of light, and so on.

Modern CCDs often boast quantum efficiencies peaking over 90%. By comparison, the quantum efficiency of the human eye peaks at approximately 1%, and the photomultiplier tube at approximately 10% [4] (Howell, 2000). Although for a given device, the quantum efficiency is assumed to be uniform across all CCD pixels, this is, of course, not realistically the case. Variations in quantum efficiency from pixel to pixel are about 1% RMS, and it is this systematic variation, along with discrepancies in pixel size that contribute to the pixel response non-uniformity (PRNU) scientists aim to correct for using flatfield images.



### 3.4 Saturation and Pixel Overflow

Once charge has been generated within a pixel, either by thermal excitation or by interaction with incoming photons, it is held in place for the duration of the integration period by an applied potential. These potential wells have a set, finite depth, and the amount of charge that can be stored in each pixel during routine operation is termed the “full-well depth”. If more electrons are generated than can be contained within a pixel, the pixel will saturate at the full-well depth and some left over charge carriers will be lost while others will overflow into neighboring pixels. The result is a widening or distortion of the point spread function, which will negatively impact photometry of this object. The point spread function, or PSF, is the intensity vs. position distribution profile of photons across the pixels of a CCD due to a distant point source (in this case, a star).

Charge-carriers can be lost from unsaturated pixels as well due to charge diffusion and charge transfer inefficiencies. Charge diffusion is the migration of electrons during integration into neighboring pixels by means of tunneling or finding defects in the silicon material. The probability of charge diffusion can be decreased by increasing the height of the potential well holding the charges in place. Shifting between clock voltages in a systematic way allows a CCD to be read out along a row or column. For each pixel, the transfer process is similar to picking up a bucket of water and dumping it into another and has similar drawbacks. Largely, each time the process is repeated, there exists a finite probability of charges being lost or left behind. A CCD with a poor charge transfer efficiency (CTE) will exhibit a streak, or tail, trailing from bright objects opposite the direction of readout. Luckily, modern CCDs generally have CTEs greater than or equal to 99.9995%, and this effect can, for the most part, be ignored.

### 3.5 Readout Noise

During readout, the accumulated charge within a pixel is first transferred to the serial register, a row of inactive pixels whose sole function is to assist in the readout process, and then the signal is sent to be amplified and converted into a digital number. The amplification is facilitated by an on-chip amplifier and the conversion by a device termed the analog-to-digital converter. The noise acquired by the signal as it makes its way through the processing electronics is random on a per pixel basis and establishes the noise floor for a CCD device. Readout noise is the term given to

the total error introduced by this whole family of contributors. One of its components is Johnson Noise, or thermal noise generated by the amplifier and other electronics, which obeys the relation [11] (Nyquist, 1928),

$$\sigma_{e^-}^2 = 4k_B T B R_{out} \quad (5)$$

Here,  $\sigma_{e^-}$  is noise in electrons,  $k_B$  is the Boltzmann constant,  $T$  is the temperature,  $B$  is bandwidth in Hz, and  $R_{out}$  is the effective resistance of the device. The only other noise I will mention here is “flicker noise”, also known as “1/f” noise for its inverse power-law dependence on frequency. It is present in almost all electronic systems and has been documented even in biological and geological phenomena. “1/f” noise dominates readout noise in devices with slow read rates ( $f_{read} < 1$  MHz). Its origins are as of yet unconfirmed, although various hypotheses have been put forth [8] (Lundberg, 2002).

For our purposes, we will treat read noise wholistically and as a constant, random, source of error in our analysis. Like all other errors along the signal path, we will look to characterize it experimentally, and minimize its effect on photometry.

### 3.6 Gain and A/D Converter Nonlinearity

Our final note on error contributions belongs to systematic nonlinearity in the A/D converter. Integral nonlinearity specifically is of interest to our project. To understand why it is so insidious, it is necessary first to introduce the concept of gain. The gain of an A/D converter is the conversion ratio between the signal in electrons and the output in ADU’s or Analog-to-Digital Units, and is set by output electronics starting with the on-chip amplifier.

$$\text{Gain} = \frac{\# e^-}{\text{ADU}} \quad (6)$$

The gain of most CCD electronics is between 1 and 20 electrons per ADU. The relationship is linear, i.e. the gain is constant, over nearly the full output range of the A/D converter. The linear region is the useable dynamic range, where a value in ADU can be easily associated with the number of charge carriers generated within a pixel. For pixels near but below saturation, however, the behavior is harder to predict, we’ve entered the region of nonlinearity. While there are clear signs which alert us to the likelihood of saturation in the A/D converter and pixel full well, nonlinear pixels raise no red flags. An experimenter who converts the value in ADUs of these nonlinear

pixels into electrons using the gain as the conversion factor would get systematically erroneous results. It is often best to avoid working in this region altogether. For example, in a 15-bit A/D converter, the largest usable output is usually taken to be around 25,000 ADU [4](Howell, 2000).

### 3.7 Error Propagation Formula

Propagation of random errors on statistically independent quantities is governed by the very important error propagation formula. I will repost it here because of its centrality to much of our analysis. Given a function  $f(x_1, x_2, \dots)$  of independent variables  $x_1, x_2, \dots$  with associated uncertainties  $\sigma_{x_1}, \sigma_{x_2}, \dots$ , the uncertainty on  $f$ , represented by  $\sigma_f$  obeys [2]

$$\sigma_f^2 = \left( \frac{\partial f}{\partial x_1} \right)^2 \sigma_{x_1}^2 + \left( \frac{\partial f}{\partial x_2} \right)^2 \sigma_{x_2}^2 + \dots \quad (7)$$

All the errors given above can be thought of as associated with independent variables.

## 4 Means and Methods

### 4.1 Data-Taking Strategy

#### 4.1.1 Equipment and Set-up

The investigation is conducted using equipment and facilities belonging to the MIT CCD Laboratory located on the fifth floor of the Kavli Center for Astrophysics Research (Building 37) at MIT. We gather data using a  $2000 \times 4000$  pixel back-side illuminated frame transfer CCD manufactured by Lincoln Laboratory. Pixels are 15 microns on a side. Electronics are designed by the MIT CCD Laboratory for use with an 18-bit A/D converter (a switch from the 12-bit to the 18-bit converter occurred about halfway through this investigation, all essential measurements were repeated using the new system). We use the lower 16 bits of the A/D converter. Integration time is about 1 second per exposure. The chamber housing the CCD is kept near vacuum at  $\sim 10^{-6}$  atmospheres; we tune its temperature by careful adjustment of the flow of liquid nitrogen into the chamber. The CCD is fitted with an 85 mm, f/1.2 camera lens with an adjustable focus. One meter away, a power LED serves as our light source. It is placed behind a “star plate”, that is, a thin metal sheet dotted with



Figure 1: A FITS image of the star plate generated by the set-up described above.

precision-drilled micrometer-width holes, and together they are mounted on a 3-axis programmable motor drive capable of simulating spacecraft jitter.

The path from the star plate to the lens is shielded, to the best of our abilities, from infrared and visible light. Output from the CCD is read by a Linux machine and compiled into FITS (Flexible Image Transport System) files for subsequent analysis.

#### 4.1.2 Temperature Control

A Carbon Resistance Thermometer (CRT) placed inside the chamber near the CCD plate monitors, to good approximation given equilibrium conditions, the temperature of the plate itself. The conversion from resistance to temperature in Kelvin occurs internal to the Lakeshore temperature control device itself, while an IDL script compiles the output, recording temperature as a function of time.

Two methods for exacting control over the temperature of the CCD are used. Method one involves a heating function built into the Lakeshore device, and an internal feedback loop to activate and deactivate the heater based on the comparison of the temperature readout to a set point temperature, or “goal” temperature. Liquid nitrogen flow is steady, governed by a programmable timer which opens and closes the solenoid valve along the liquid nitrogen pipeline. The heater-timer method has the advantage of shorter period and lower amplitude temperature fluctuations in its

equilibrium state (as short as a few seconds depending on the setting on the timer, and as low as 0.2K), but has the disadvantage of direct heating of the CCD, which, depending on the location of the temperature probe relative to the active heating mechanism, may yield unpredictable results due to uneven or local heating, such as a temperature gradient in the CCD or an inaccurate temperature reading. This method runs through nitrogen at a quicker pace, which limits the total number of data points with which we can construct a stable light curve.

A second method takes input from the CRT, passes it through a simple logic circuit (Figure 2), and outputs instructions to the solenoid valve which controls nitrogen flow. It uses no heating mechanism aside from thermal contact with room temperature environment, and the set point is a range as opposed to a single value. The chamber temperature readout is compared with two bounding temperature values by way of a comparator, and the device will act to keep the temperature within this range. The range itself is set by a network of resistors and one adjustable potentiometer. This method has as its advantage even warming/cooling of the CCD and a more reliable temperature reading due to affecting the large-scale temperature control mechanism rather than combating its effects on a local scale (treating the cause, rather than the symptoms, so to speak). However, it is not without its drawbacks as the nitrogen must flow through the piping in order to begin cooling the CCD, the thermal inertia of this system is rather large and we are looking therefore at a slower response rate. Using a range of temperatures as a set point rather than a single value, although essential for the correct operation of the circuit created especially for this purpose, also acts to increase both the amplitude and the period of the temperature oscillations to approximately 1K and 3-4 minutes, respectively.

#### 4.1.3 Dark Current Elimination

The strong dependence of dark current on temperature is good encouragement to work in a very low temperature regime. Of course, since dark current is zero only at absolute zero, we are not looking to eliminate it completely. Instead, we look to establish a level for the dark current such that the shot noise resulting from the dark current is insignificant compared to the readout noise and other baseline, temperature-independent sources of noise. Figure 3 plots the total noise in an unlit region of the CCD against the temperature of the device.

It becomes immediately evident that below -110K, dark current noise disappears behind a dominant, temperature-independent noise term which is slightly larger than

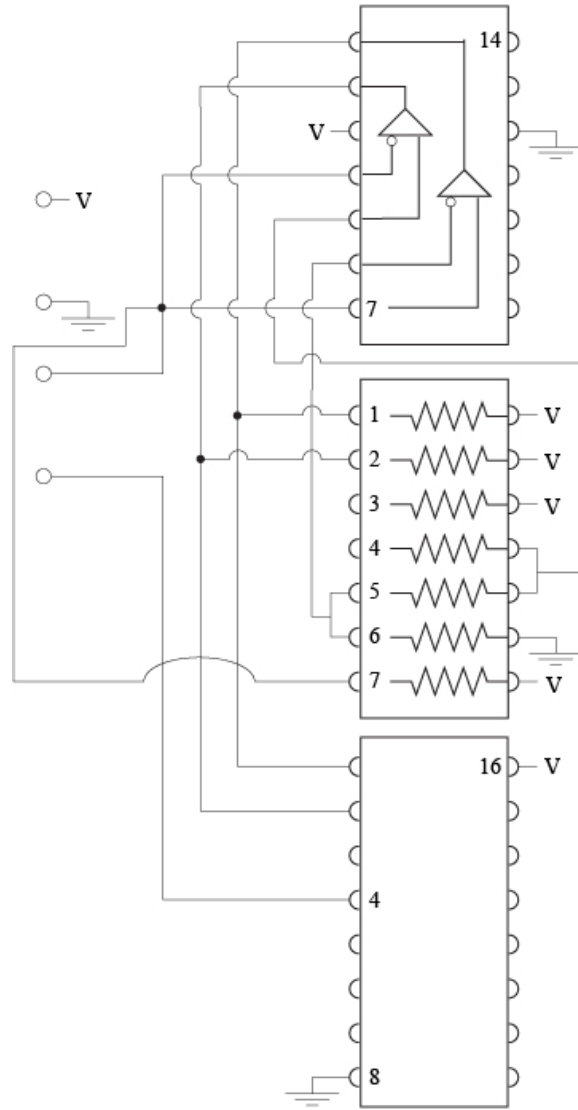


Figure 2: From the top down: LM139J, a low power low offset voltage quad comparator; seven resistors, some of which to establish set point and range; SN74LS279AN, a quadruple S-R latch.

the readout noise of the electronics as measured in the overflow region of the CCD by a fraction of an ADU. The divergence of the noise in different regions in the high temperature zone indicates structure in the CCD pixels, and the asymptotic difference between readout noise in the active region of the CCD and in the overflow region is closely related to a bias offset which for this CCD, could not be reduced any further. It is important to mention that this data is collected on a 12-bit converter and a test CCD for the purposes of developing experimental strategy early on, and the later

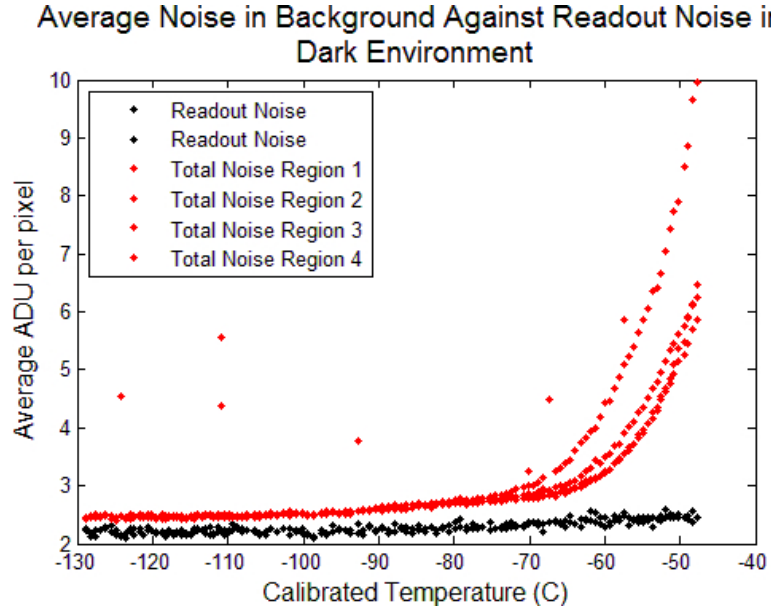


Figure 3: Comparison of total pixel-to-pixel variation of several regions in a dark frame of the CCD to the variation in the overclock region (readout noise only), as a function of approximate temperature.

photometric data is actually taken with a similar but more advanced CCD and set of electronics.

#### 4.1.4 Strategy for Dealing with Pixel-to-Pixel Variation

The measured pixel-to-pixel RMS deviation in quantum efficiency is 0.8% for the actual CCD used in the following experiment [16]. In addition there is often minor structure in the noise or the dark current generated on a per pixel basis due to variations in pixel size or in the material itself. Although seemingly insignificant, these pixel-to-pixel variations are what mandates the practice of “flat-fielding”. Flat-field images, usually taken of a uniformly illuminated surface such as a white wall, give us all the necessary information to normalize out all noise contributions of this nature from our data frames.

Because of the nature of our eventual mission, we neither have the flat-fielding capabilities we have on the ground (no moving parts on spacecraft bus, no large, uniformly lit regions in the sky) nor do we need them. We are merely looking for changes in a star’s total incident intensity. Therefore, if we can keep the spacecraft

attitude fixed to within a couple of arcseconds, we can keep the major portion of each star's point spread function (PSF) over the same few pixels, and will not need to attempt to flat-field in space. Strangely enough, we will find that our pointing accuracy and the steadiness of the attitude of the camera and CCD is probably better in space than in the lab. Nevertheless, we adopt the technique of fixing the array of stars to the same position on the grid of CCD pixels for each image as a way of eliminating pixel-to-pixel variation.

#### 4.1.5 Humidity's Effect on Photometry

During the summer months, especially, humidity is an issue in the Boston area. When untreated, condensation begins collecting on the window of the liquid-nitrogen-cooled chamber behind which is situated the CCD. Of course, water droplets deflect and reflect incident light, and the presence of this condensation can severely impact photometry. Our remedy is dry nitrogen. A steady flow of dry nitrogen over the chamber window, initiated before the liquid nitrogen, is sufficient to remove this worry from our minds.

#### 4.1.6 Stability of LED Light Source

Since every variable is a potential source of noise or error in our investigation, it is also important to be able to fully control the brightness of the power LED light source. Originally, a voltage-source circuit supplied the power to the LED and the LED was operated at the very lowest end of its capabilities due to limited full-well capacity in the test CCD and a 12-bit A/D converter. Early data showed disturbing, high amplitude, apparently random fluctuations in the brightness of stars in the star plate on the timescale of hours (see Figure 4).

After ruling out possible causes including humidity (as discussed in section 4.1.5 above) and correlations with CCD temperature, we realize the culprit is likely the light source itself and make two crucial corrections. First is the design of a very basic, constant (but tunable) current source (see Figure 6). Then, the brightness of the LED is cranked up to normal operating levels while its signal is accordingly dimmed by two constant-density filters. This allows us to continue to operate in the undersaturated regime of our instruments and stable range of our LED at the same time. Stability was much improved after these changes were implemented (see Figure 5).



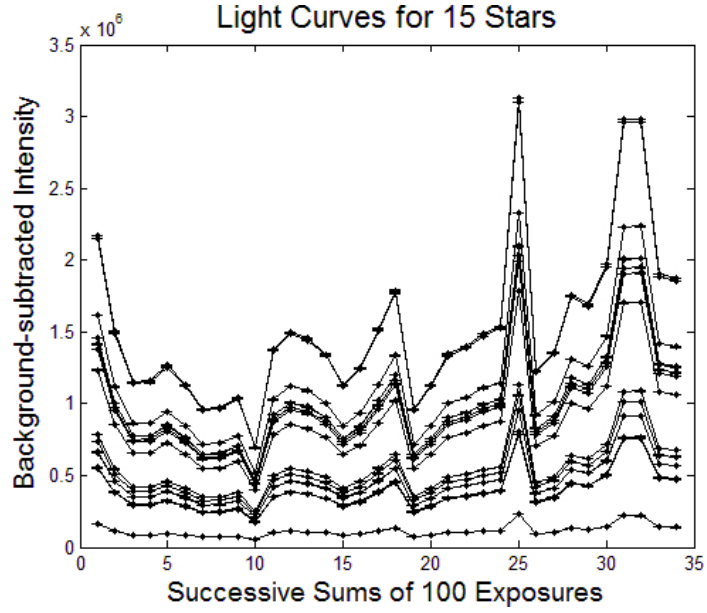


Figure 4: Early light curves for 15 stars using 12-bit electronics. Evidence of an unstable LED source.

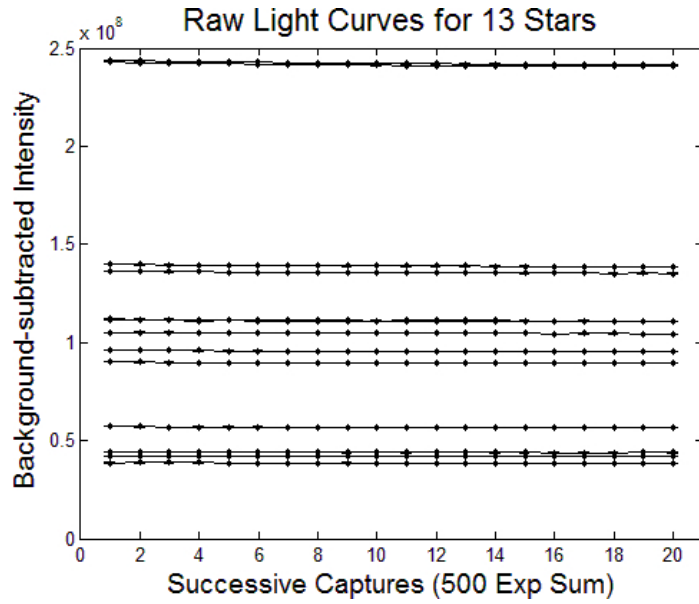


Figure 5: Light curves obtained after changes were made to the LED power source and operational parameters. No normalization has taken place.

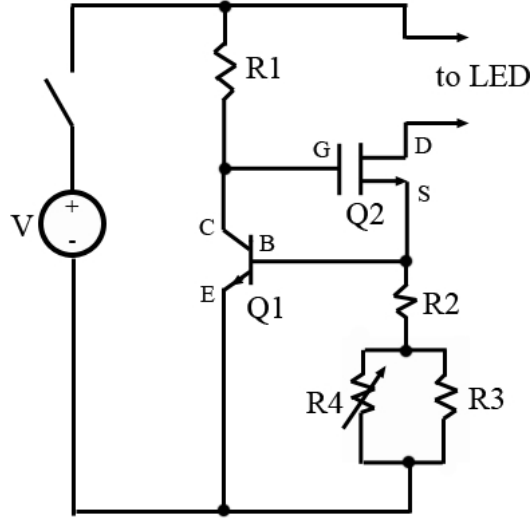


Figure 6: Constant current source circuit diagram. R1 is a 100 k $\Omega$  resistor, R2 a 120  $\Omega$  resistor, R3 a 1 k $\Omega$  resistor, R4 a 5 k $\Omega$  potentiometer. Q1 is an NPN transistor, Q2 is an N-channel MOSFET.

#### 4.1.7 Undersaturating Pixels and A/D Bits

We take pains to avoid saturating the full-well of a pixel or the A/D converter in order to avoid many of the problems introduced in Section 3 which become manifest in this region. Our strategy in general will be short exposures and low-intensity signals, and relying on stacks of individual image frames to produce the statistics necessary to reach our photometry goals.

## 4.2 Analysis Strategy

### 4.2.1 Image Stacking and Stamp-Size Subarrays

FITS format output produced in the readout process is an array of signal values in ADUs which preserves the location of the pixel on the CCD that had collected it. This makes image stacking a simple task, as the value of a particular pixel in any exposure can be found each time at a fixed location in the array. Analysis scripts are equipped with the ability to take simple sums over many FITS arrays along each element in the array in order to produce stacked images which hopefully reproduce the photometry of much brighter objects.

An onboard data reduction technique planned for TESS, which would reduce dramatically the data downlink load, is the use of image subarrays. Eventually, a

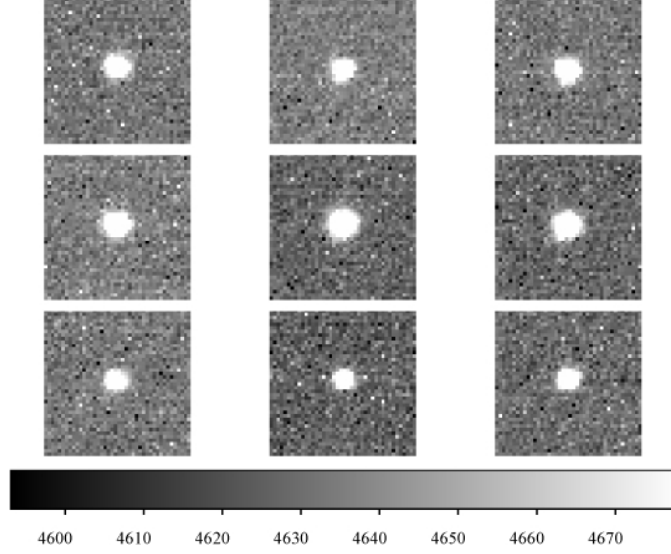


Figure 7: 40x40 pixel subarrays generated from full CCD frame.

program will locate the centers of stars suitable for photometry, draw a certain sized box around it, and save only these stamp-size arrays for analysis. For now, we choose the star centers by hand, since this only needs to be done each time the star plate is shifted, and leave the rest to a computer script.

The script reads in the list of star centers, takes 20 pixel-steps in each direction from these locations, and throws down a  $40 \times 40$  pixel frame around each star of interest. These subarrays are saved in a separate file for subsequent analysis. An example of nine stamp-size subarrays is shown in Figure 7.

#### 4.2.2 Background/Bias Subtraction

There are many ways of finding the background-subtracted intensity of a star in a subarray. For very precise measurements, one may desire to fit the point spread function of the signal on the CCD to a gaussian, or even better, an Airy disc for diffraction through a circular aperture, defined by

$$I(r) = I_0 \left( \frac{2J_1(\alpha r)}{\alpha r} \right)^2 \quad (8)$$

where  $J_1$  is the first order Bessel Function, and  $I_0$  and  $\alpha$  are fit parameters. There is much complexity to PSF fitting and it is even more complicated by the distortion of the PSF due to non-central location in the field of view, an example of which is

given below in Figure 8, data from Howell, 1996 [4]. For our current purposes, the marginal improvement in photometry is not worth the added processing time and complication; instead, we go with a simple sum. The program finds the peak pixel in

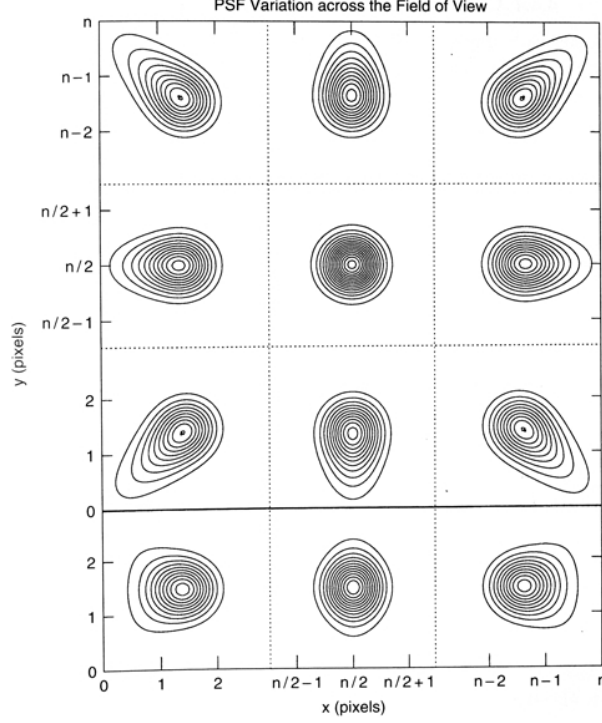


Figure 8: The PSF of a single star deviates from circular symmetry when its location on the CCD is non-central. Bottom row is sum of the PSFs along each column. From Howell, *et al*, 1996.

each subarray and draws another bounding box of specified radius  $b$ . It then sums the values of all the pixels contained within this smaller photometry box. To determine background, it does a 300 pixel sample of the perimeter of the subarray and calculates the average value of these pixels “far away from the star”. This same value is then subtracted on a per-pixel basis from the signal pixels within the central photometry box. The operation is summarized below, where  $I_{bs}$  is the resulting background-subtracted intensity of the star.

$$I_{bs} = \sum_{i=0}^{4b^2} S_{ph,i} - 4b^2 \bar{S}_{bg} \quad (9)$$

Here,  $S_{ph,i}$  is the signal (in ADU) collected from the  $i$ th pixel within the photometry box of radius  $b$ , and  $\bar{S}_{bg}$  is the average background level set by a sample of 300 pixels

along the perimeter of the full  $40 \times 40$  subarray.  $4b^2$  is just the total number of pixels. This method eliminates the need to take bias or dark frames, and allows us to observe parts of the sky with very different temperatures and background photon levels at the same time. With a consistent method of simultaneous local background and bias correction, the mission is afforded a greater observing flexibility and freedom.  $S_{ph,i}$  has two main contributions that we need to be concerned with, incident photons and bias. The uncertainty on  $I_{bs}$  can then be found by using the error propagation formula, Equation 7, assuming shot noise error on the actual bias-subtracted signal and approximately uniform illumination of each background pixel.

$$\sigma_{I_{bs}} = \sqrt{I_{bs} + 4b^2\sigma_R^2 + 16b^4\sigma_{\bar{S}_{bg}}^2} \quad (10)$$

The error on the mean background depends on the readout noise  $\sigma_R$  and the number of pixels used in the calculation,  $N$ .

$$\sigma_{\bar{S}_{bg}} = \frac{\sigma_R}{\sqrt{N}} \quad (11)$$

Equation 10 becomes:

$$\sigma_{I_{bs}} = \sqrt{I_{bs} + 4b^2\sigma_R^2 \left(1 + \frac{4b^2}{N}\right)} \quad (12)$$

Later,  $b$  will be optimized for signal-to-noise ratio, or  $I_{bs}/\sigma_{I_{bs}}$ .

### 4.2.3 Star Field Intensity Profile and Relative Photometry

Relative photometry is a useful technique for eliminating wide-field fluctuations in signal intensity. Though it is more crucial in ground-based exoplanet surveys than in space, it is useful in all contexts involving electronics as it removes the effects of common-mode rejection in amplifiers [7], which uniformly affects all signals. We will find that in our investigation, in particular, due to the nature of our light source, it is indispensable. We model our light source as an isotropic emitter. A diffuser is placed a distance  $d \approx 1.5$  cm away from the source, and the star plate approximately 2 inches from the diffuser. It is immediately obvious our star field will not be uniformly illuminated. The brightness profile of the stars on the star plate will mirror the distributed intensity of light incident on the diffuser placed behind it. Ideally, as a function of polar distance  $\rho$  from the centroid of the symmetric profile ( $\vec{x} = (0,0,0)$  in our coordinates), intensity  $I$  is described by the function

$$I(\rho) = \frac{P_{tot}d}{4\pi} \frac{1}{(d^2 + \rho^2)^{3/2}} \quad (13)$$

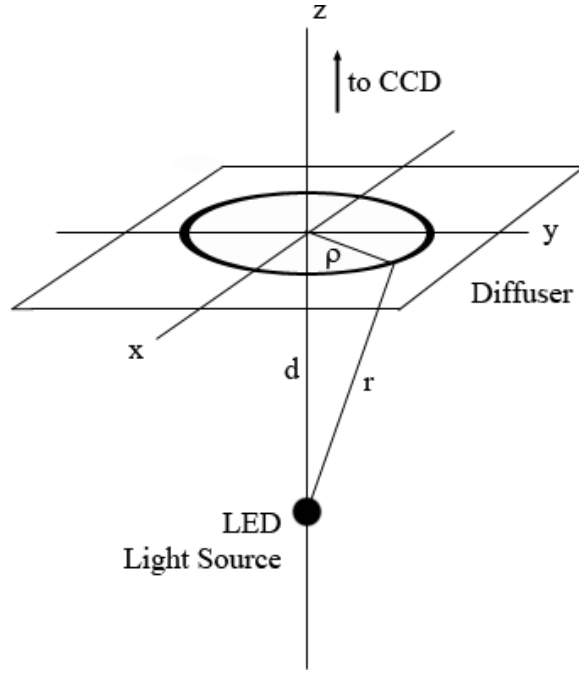


Figure 9: Geometry and coordinate designations used to calculate intensity profile for stars in star plate as a function of  $\rho$ , distance from the  $z$ -axis.

where  $P_{tot}$  is the total power radiated by the LED light source. A plot of a cross section of this intensity profile as a function of distance from the  $z$ -axis is shown in Figure 10.

This function is linear in  $P_{tot}$ , which tells us that a constant factor increase in the brightness of the LED results in the same constant factor increase in the brightness of every star in the star field. Fluctuations of this nature can be corrected for by relative photometry.

Relative photometry is normalized photometry. Each star's total signal in electrons is converted into a unitless ratio by comparing its value against some reference value. There is some freedom in the choice of this reference, and clearly some choices are better than others. For one, it should not be a constant, but vary accordingly with the stars in the field. It should be some reliable characterization of the overall photometry. For these reasons, we choose as our reference value the average intensity of all stars of photometric interest in the frame.

$$R_i = \frac{I_i}{(1/M) \sum_{j=1}^M I_j} \equiv \frac{I_i}{\bar{I}} \quad (14)$$

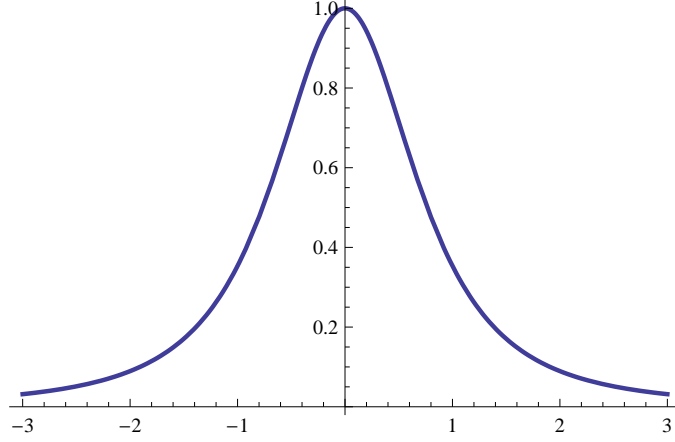


Figure 10: Projected intensity of light onto a planar diffuser from an isotropic source as a function of radial distance  $\rho$ . The profile is reflected across the vertical axis to emphasize circular symmetry.

$R_i$  is the relative brightness value of star  $i$ ,  $I_i$  is brightness in electrons,  $M$  is the number of relevant stars in the field. The uncertainty on  $R_i$ , propagated using Equation 7, is then

$$\sigma_{R_i} = \sqrt{\left(\frac{1}{\bar{I}}\right)^2 \sigma_{I_i}^2 + \left(\frac{I_i}{\bar{I}^2}\right)^2 \sigma_{\bar{I}}^2} \quad (15)$$

with  $\bar{I}$  representing average intensity. Putting them together to find an expression of normalized noise introduced by this method of photometry, we find,

$$\sigma_{R_i}/R_i = \sqrt{\left(\frac{\sigma_{I_i}}{I_i}\right)^2 + \left(\frac{\sigma_{\bar{I}}}{\bar{I}}\right)^2} \quad (16)$$

$\sigma_{I_i}$  is calculated by the photometry software alongside  $I_i$ ,  $\sigma_{\bar{I}}$  is given below.

$$\sigma_{\bar{I}} = \frac{1}{M} \sqrt{\sum_{j=1}^M \sigma_{I_j}^2} \quad (17)$$

These equations are central to our strategy of relative photometry. As an aside, if we assume Poisson statistics (which is very idealized, of course), the relative signal to noise ratio,  $\sigma_{R_i}/R_i$ , reduces to

$$\sigma_{R_i}/R_i = \sqrt{\frac{1}{\bar{I}} \left( \frac{1}{R_i} + \frac{1}{M} \right)} \quad (18)$$

We confirm the intuitively reasonable assumption: that the photometry is limited by the number of stars,  $M$ , involved in the mean. In order to control the error introduced by normalization,  $M$  should be as large as possible.

### 4.3 Summary

We have most of the tools we need to begin our study. The code required to implement the functions described above is written in a number of languages, including Matlab, IDL, C, and Shell script. It's important, however, before we begin, to review the procedure as it has been presented so far as well as introduce the desired format for our results. Light travels from the light source to the diffuser, through the holes in the star plate, along a light-shielded path, into the lens which focuses the photons onto the pixels of a CCD in back. The CCD is held at a temperature of -120K or below and read out approximately every second. The electrons collected in each pixel are transferred and converted by an A/D converter into ADUs and stored in FITS files for analysis. Analysis begins by stacking the images in chronological order in groups of 500 or more for improved statistics. Star centers are picked out and subarrays generated for each star in each stacked frame to facilitate data transfer and storage. Each star has an absolute and relative brightness in each frame sum, which is to be compared with its own values at earlier and later times. An RMS deviation of the relative intensity is measured, and inspected for its resemblance to expected error ( $\sigma_{R_i}$  calculated from the parameters of the experiment) and shot noise limit of each particular star. Finally, all these uncertainty values are given as fractions of the average intensity of the star, multiplied by  $10^6$  to give parts per million statistics.

## 5 Calibration - CCD Gain

As with any experiment, calibration of the equipment is essential before any interpretation or analysis of the data can take place. A parameter of utmost importance when working with output from CCD electronics is gain. A more detailed introduction to gain can be found in Section 3.6, but suffice to say, it is most straightforward and reliable to determine the gain of the system by measurement rather than calculation.

Several established methods exist. I will describe two of the simplest and one of those in detail as it is carried out.



## 5.1 Relation to Shot Noise of a Bright Source

The first of these methods takes advantage of shot noise statistics and the relationship between number count of incident photons and numerical output in ADU. In the visible light and infrared region of the spectrum, one photon is universally correlated with the creation of one electron-hole pair [14]. The conversion between units of ADUs and photon counts is then,

$$N_{ADU} = N_{\gamma}/g + Bias + N_{DC}/g \quad (19)$$

where  $g$  is the gain of the system. Bias is in units of ADU, and dark current,  $N_{DC}$ , in units of electrons to facilitate in calculation of Poisson noise (see Section 3.2). Since the number of photons obeys shot noise statistics, we can calculate the noise per pixel in ADU,  $\sigma_{ADU}$ . It is a function of photon signal,  $N_{\gamma}$ , readout noise in electrons,  $\sigma_R$ , and dark current in the pixel,  $N_{DC}$ .

$$\sigma_{ADU} = \frac{1}{g} \sqrt{N_{\gamma} + \sigma_R^2 + N_{DC}} \quad (20)$$

in the region where  $N_{\gamma} \gg Bias$  and  $N_{DC}$ , Equation 19 reduces to

$$N_{ADU} \approx N_{\gamma}/g \quad (21)$$

and the noise becomes

$$\sigma_{ADU} \approx \frac{1}{g} \sqrt{N_{\gamma}} \quad (22)$$

converting  $N_{\gamma}$  in photons into units of ADU we plug Equation 21 into Equation 22 and obtain

$$\sigma_{ADU} \approx \frac{1}{g} \sqrt{g N_{ADU}} = \sqrt{\frac{N_{ADU}}{g}} \quad (23)$$

which is decidedly *not* Poisson in nature unless  $g = 1$ .

This key relationship can be exploited to determine the gain,  $g$ , from histograms of pixel values by analyzing either one very bright, very uniformly illuminated flat field frame, obtaining  $\sigma_{ADU}$  from the RMS variation from pixel to pixel, and  $N_{ADU}$  as the mean value of all pixels, OR taking multiple exposures of a single, steady, bright source, and extracting  $\sigma_{ADU}$  and  $N_{ADU}$  from single pixel variation from frame to frame.

We went into a bit of detail in discussing this method because of the important relations introduced. Equation 20 in particular, is the crucial noise component of the

ubiquitous “CCD Equation”, in units of electrons,

$$\frac{S}{N} = \frac{N_\gamma}{\sqrt{N_\gamma + N_{DC} + \sigma_{Re}^2}} \quad (24)$$

## 5.2 Calibrating to X-Ray Photons of Known Energy

Scholze, *et al*, found in 1996 [14] that the average electron-hole pair creation energy in silicon is 3.64 eV for excitation by photons in the x-ray range. Iron-55 decays into manganese-55 by inner-shell electron capture and the resulting cascade of higher energy electrons into lower energy orbital states to fill in the ground state of the manganese atom releases a bundle of x-rays with highly specific energies. The  $K_\alpha$  line emitted by the decaying Fe-55 atom corresponds to the  $2p \rightarrow 1s$  transition and has an average energy of 5.9 keV. The  $K_\beta$  line corresponds to the  $3p \rightarrow 1s$  transition and has an average energy of 6.5 keV [10]. The corresponding number of charge carriers created by the absorption of a single x-ray photon is then 1621 and 1786 respectively. If we then measure the ADU signal output by the CCD corresponding to these individual events, we can very easily take their ratios and obtain the gain of the system.

The front plate to the vacuum chamber containing the CCD is removable and interchangeable. For photometry purposes, the front plate is fitted with a camera lens to focus photons from the light source onto the CCD. For gain determination, this front plate is removed and replaced with one fitted with an Fe-55 x-ray source. The chamber is light sealed with the exception of the x-rays. A 1 second integration of a portion of the illuminated CCD is shown in Figure 11.

A single absorption event on the CCD shows up in the read out in several common ways, see Figure 12. All the energy of the photon is either absorbed by one pixel (single-pixel event), or it is spread out among several neighboring pixels (multiple-pixel event). This means, any pixel participating in an event can contain anywhere from 0 to 1621 (or 1786) electrons. Since the sum across all pixels in an event should reflect the total energy of the photon impact, some scientists opt to create scripts which would identify single and multiple pixel events and sum them to produce the total signal in ADU. A histogram is then created depicting the distribution of this signal sum across all identifiable events. Hopefully, the statistics will be normally distributed. A gaussian fit then reveals the mean.

Unfortunately, the few times we tried, this procedure did not produce much in terms of identifiable peaks. We reverted to a much simpler approach, which actually

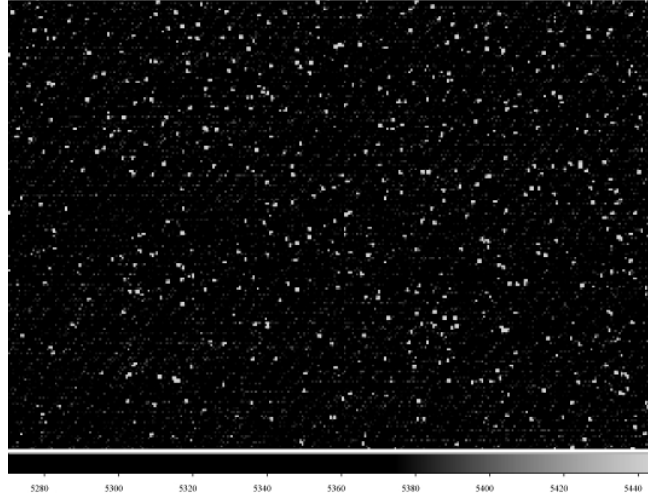


Figure 11: A portion of the CCD illuminated by x-rays from Fe-55 source.

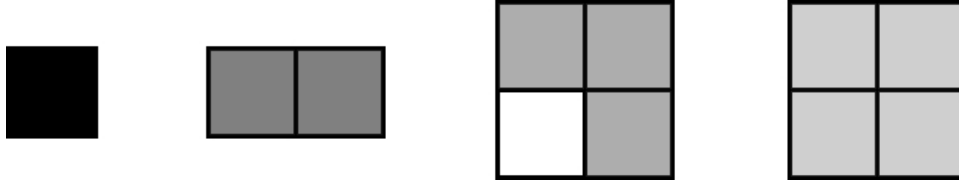


Figure 12: From left to right: a single pixel event, followed by 2-, 3-, and 4- pixel events. The signal is pictured as being evenly distributed among the individual pixels but this is not necessarily the case.

turned out some clearer results.

Although any pixel involved in an event is more likely to contain some of the energy rather than all, when arranged in terms of signal values and frequency of occurrence, a pixel is more likely to report the value associated with a single-pixel event than any other specific value. In addition, we expect a step-like behavior, such that above certain energy thresholds, more precisely, the two main energy values taken on by the photons, the count will drop significantly as possible contributing photons diminish. Any signal above the energy of the  $K_\beta$  peak is either from even more energetic transitions or cosmic rays.

The histogram in Figure 13 is produced from the individual pixel values obtained in 100 exposures (not stacked), with bias determined by a gaussian fit to the zero-signal (largest) peak and subtracted individually from each frame. Individual peaks

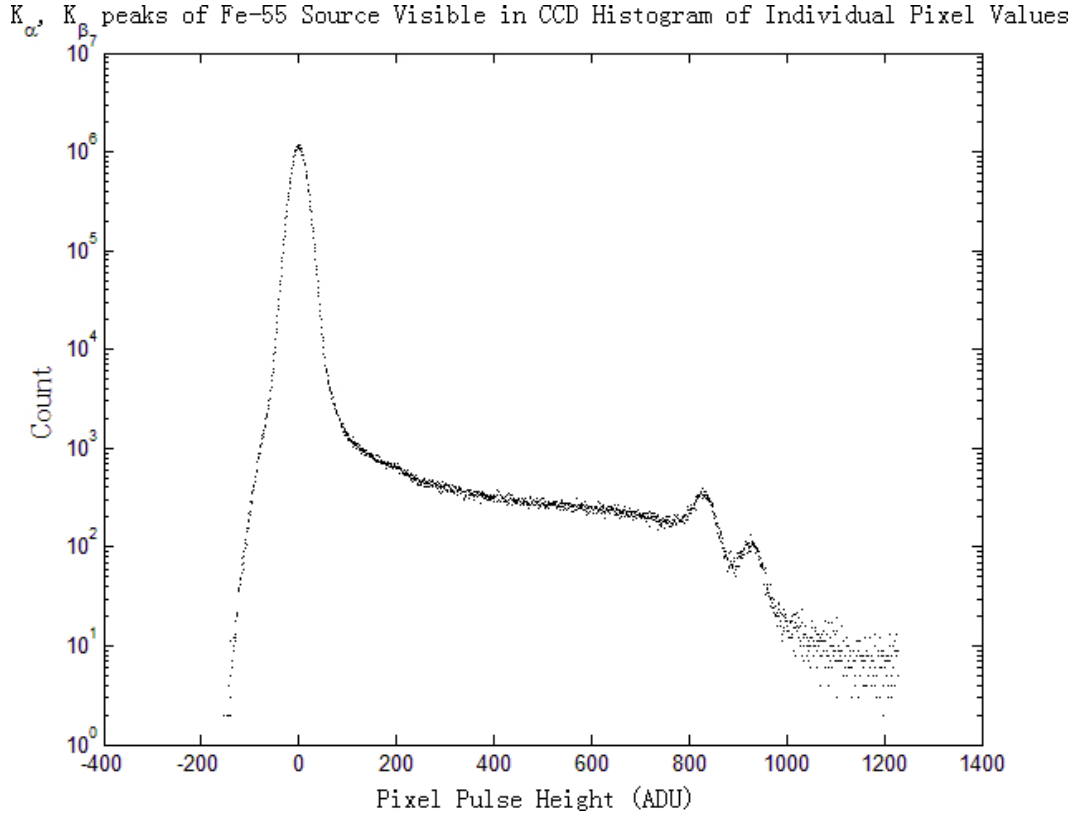


Figure 13: Histogram of count against pixel value (in ADU) in x-ray calibration exposures. The  $\text{Mn-55 } K_\alpha$  and  $K_\beta$  peaks are clearly visible. The largest peak centered at 0 ADU is the result of bias subtraction. The readout noise is measured to be 28.4 electrons.

are fit to gaussian functions, their means extracted. The width of the bias peak at 0 ADU is a good indicator of readout noise, which in this case is 14.2 ADU. Figure 14.

$$1620/(824 \pm 10) = 1.97 \pm 0.02$$

$$1786/(921 \pm 15) = 1.94 \pm 0.03$$

We find the gain of the system to be around  $2 e^-/\text{ADU}$ . The readout noise in electrons is then a very high 28.4.

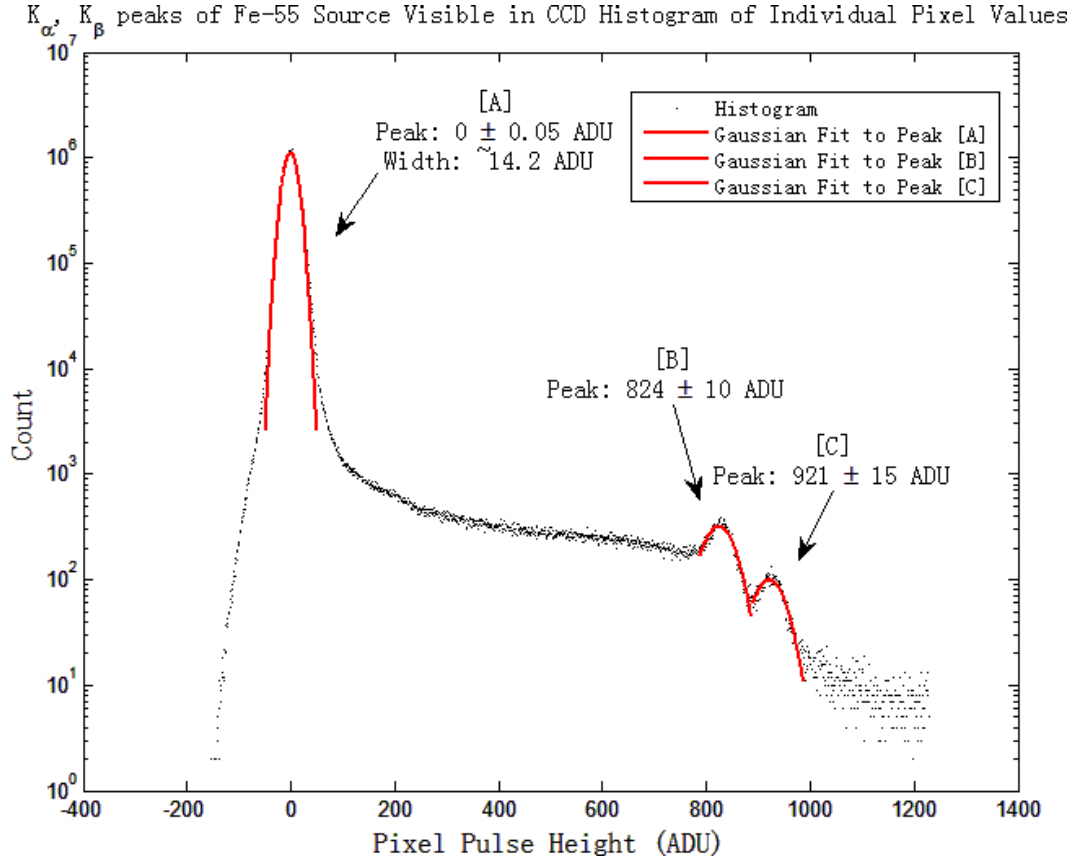


Figure 14: Several gaussian fits are plotted over the histogram. Peaks are at 0, 824, and 921 ADU. Peak [A] is the bias, peak [B] corresponds to the  $K_{\alpha}$  line of Mn-55, and peak [C] to the  $K_{\beta}$  line.

## 6 Photometry

### 6.1 Star Plate Layout and Star Reference Numbers

For the purposes of photometry, we are most concerned with stars near the center of the field of view. PSF aberration is lowest in this region (Figure 8), and brightness most uniform among the stars (although as we see it is still not very uniform at all). We window only the region of the CCD which contains our stars of interest. The motivation is reduced requirements on processing time and disk space. The windowed region is shown in Figure 15 with the candidate stars labeled by number.

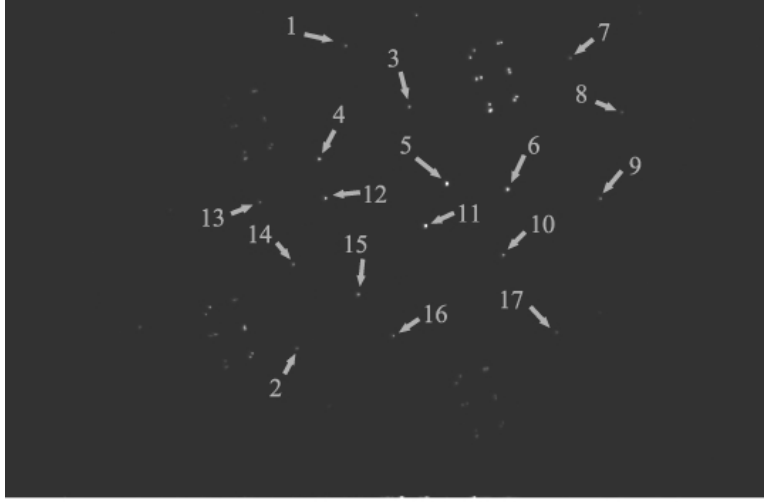


Figure 15: Candidate stars participating in photometry are referenced by number in no particular order. Brightest stars are near the center of the distribution.

## 6.2 Signal to Noise as a Function of Bounding Radius

In Section 4.2.2, we discussed our strategy for extracting absolute intensities of stars by the use of bounding boxes and background subtraction. If you recall, our scripts locate the brightest pixel in a stamp size subarray and draws a bounding box of radius  $b$  around it, considering as signal only the pixels contained within this box, and subtract from it the background and bias contributions in order to determine background-subtracted intensity.

Thus, the choice of  $b$  plays a major role in the level of photometry we can hope to achieve. Thinking about limiting cases only, it makes intuitive sense that as  $b$  approaches zero, our signal to noise will drop to zero. On the other hand, as  $b$  approaches the radius of the subarray, signal will stay constant as noise increases (Equation 12), and signal to noise will decrease. A continuous function that increases then decreases will have a maximum somewhere in between, we can optimize statistics while holding all other parameters constant if we operate at this  $b_0$ .

The value of  $b_0$  depends on the width of the point spread function. Therefore, we seek to determine  $b_0$  experimentally by comparing the value of  $I_{bs}/\sigma_{I_{bs}}$  for increasing values of  $b$ .

We verify the behavior we expect based on the parameters we were handed. We find that most stars peak at a relatively large  $b = 9$  while the brightest stars peak at

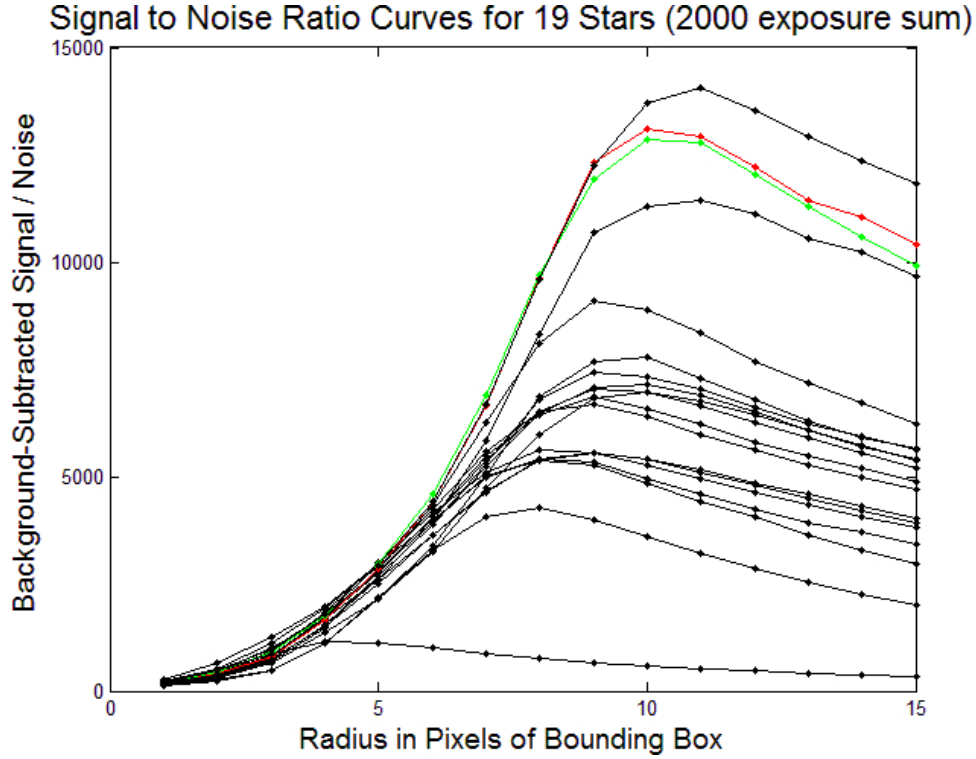


Figure 16: Signal to noise ratio as a function of bounding box radius  $b$ , stars of different brightness seem to peak at different values of  $b$ .

an even larger radius. Since their photometry is not much compromised, we choose  $b_0 = 9$  for subsequent photometry operations on all stars in the frame. We can be assured that as long as the light source, the focus, and the integration time are all kept relatively stable, we will not need to repeat this analysis.

### 6.3 Intensity Correlations with Temperature and Position

In the course of our study we ran into a very strange correlation between temperature of the CCD and the x-y location of the centroid of the star on the pixels of the CCD. We learn from our analysis (Figure 17) that this fluctuation was on the order of a tenth of a pixel, and the orientation of this motion was different enough from star to star to lead us to believe that it was the result of a rotation of the CCD.

At the time we were using the external temperature control circuit and the heater was off. The temperature oscillated periodically between the two preset turning points with a period of approximately 3 minutes and an amplitude of one degree. We were

skeptical that a change in one degree would result in such a noticeable rotation of the CCD in the chamber, but noticing an asymmetry in the shape in the periodic deflection, realized it must be correlated with the on/off action of the nitrogen rather than the temperature measured on the CCD itself.

The chamber is fed by a flexible metal hose which is affixed to the side of the CCD. Although the period of their oscillations will be the same, the hose which is in direct contact with the nitrogen is subject to much greater extremes of temperature than is the near equilibrium of the chamber. Large and sudden swings in temperature have a dramatic effect on material properties, a small tensing of the tube is enough to generate jitter at the level we observe.

Much more troubling is the effect of this jitter on photometry, as it was much more pronounced than would be predicted by mere pixel-to-pixel variation in quantum efficiency. Photons from a bright star are spread out over many pixels (its photometry is built from 81, for instance), the worse case scenario is that all these pixels are unique from frame to frame, corresponding to a jitter of more than 18 pixels. In that case the variation in photometry due to pixel response non-uniformity will be on the order of  $1\%/\sqrt{81}$ , or 0.1% [15]. Our observed brightness fluctuations for the star whose statistics are given in Figure 17 is an order of magnitude greater, while our measured jitter is more than two orders of magnitude below that which is used in this calculation. When we look away from the bright stars, we see this effect disappear entirely behind shot noise, Figure 19, which hints that this is likely an issue associated with saturation. A more detailed look at a fainter star can be found in Figure 18.

We speculate that there is clipping of the bright pixels or other loss of charge associated with nonlinearity.

As the stars move around, the point spread function remains approximately constant while the pixels shift underneath it. This could make the difference between distribution of peak intensity over several pixels and a situation where the peak value falls squarely on one pixel. In the latter case, clipping (or charge loss) would be more severe, and a dip would be seen in the light curve of the integral intensity of the star each time it oscillates between these two states.

Toning down the light levels and excluding from our photometry the brightest stars that exhibit this phenomenon, we ultimately construct a seven point light curve based on stacks of 2000 images.



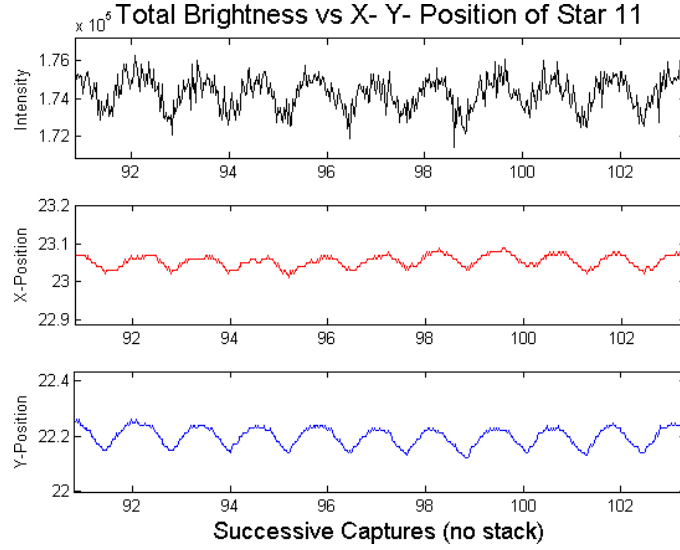


Figure 17: Temperature-correlated periodic displacements in centroid position of a bright star on the CCD. Because the star is near saturation, we observe that its background-subtracted intensity is highly impacted by this small change in position.

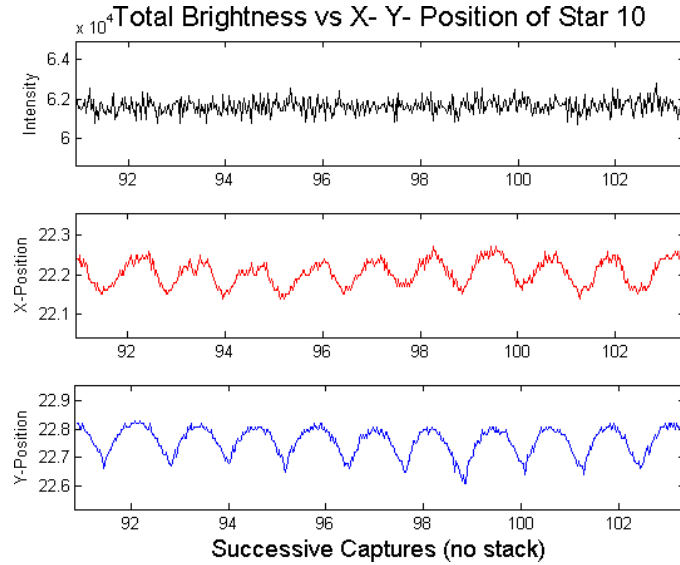


Figure 18: The intensity of fainter stars appear to be uncorrelated with movements on the order of a tenth of a pixel.

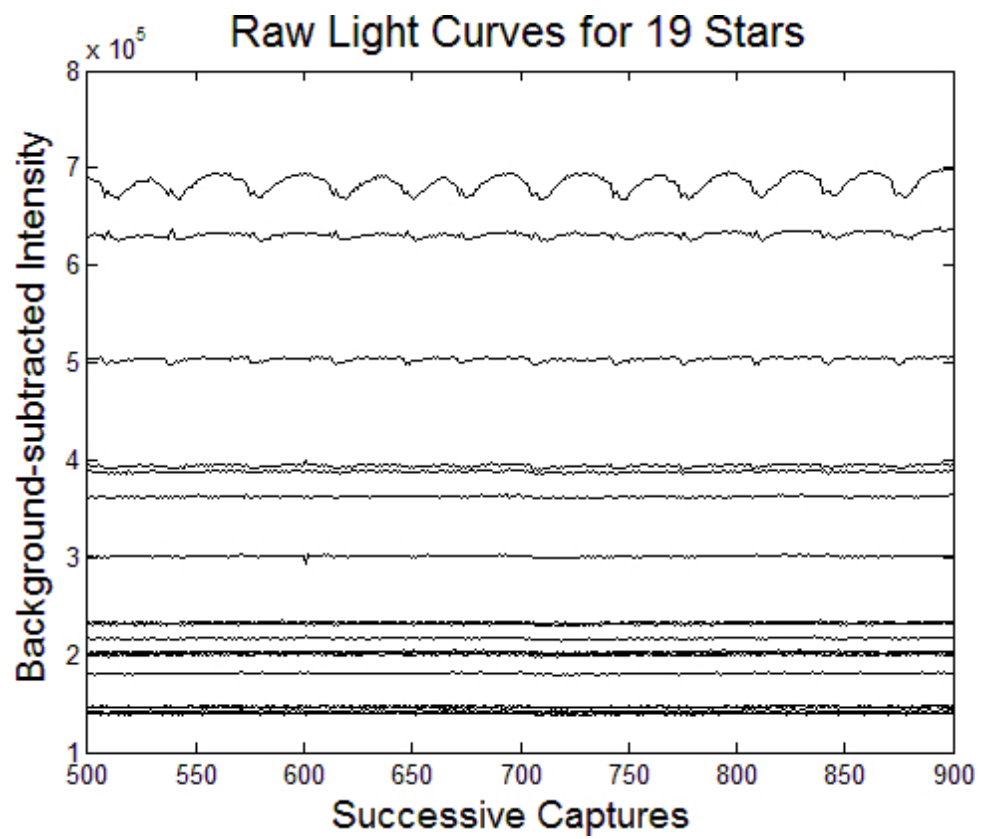


Figure 19: Brighter stars are disproportionately affected by this anomalous intensity-position coupling.

## 6.4 Light Curves

### 6.4.1 Shot Noise Limit?

With such a high readout noise level ( $\approx 28.4$  electrons, Figure 14), we struggle to reach shot noise limited photometry. We modify Equation 12 to find  $\sigma_{I_{tot}}$ , the photometric noise when working with stacks of  $\eta$  images with constant intensity,  $I$ , in each frame. We drop the background-subtracted subscripts for clarity's sake, as it is assumed that all stellar intensities are background-subtracted. The major adjustment is the dependence on  $\eta$ ,

$$\sigma_{I_{tot}}(\eta) = \sqrt{I\eta + 4b^2\eta\sigma_R^2 \left(1 + \frac{4b^2}{N}\right)} \quad (25)$$

With  $b = 9$ ,  $\sigma_R \approx 28$  electrons,  $N = 300$ , and  $\eta \approx 2000$ , the contribution from the second term in the equation is on the order of  $1 \times 10^9$  electrons. In order to reach shot noise limited photometry, where  $\sigma_{I_{tot}} \approx \sqrt{I_{tot}}$  and  $I_{tot} = \eta I$ , we would need to collect  $I_{tot} \gg 1 \times 10^9$  electrons. If we attempt to accomplish this by frame stacking, doubling  $\eta$  would double the intensity, but at the same time would double the readout noise component under the radical, and their contributions to the total noise remain at the same proportion as before. This implies stacking is generally ineffective for the purposes of bringing our stellar photometry closer to the shot noise limit. However, all is not lost. Meanwhile, the ratio  $\sigma_{I_{tot}}/I_{tot}$ , our fractional noise, does decrease as  $1/\sqrt{\eta}$ , so stacking has a positive effect on our photometry in the expected way.

$$\sigma_{I_{tot}}/I_{tot} = \sqrt{I + 4b^2\sigma_R^2 \left(1 + \frac{4b^2}{N}\right)} \frac{1}{I\sqrt{\eta}} \quad (26)$$

All of this is easy to see graphically. Figure 20 compares our fractional noise (Equation 26) with shot noise statistics as a function of  $\eta$ , the number of frames in a stack. Approximate values were entered for all constant parameters.

### 6.4.2 Exclusions

Although, due to the high readout noise of the system, we cannot hope to get any nearer to the shot noise limit by summing, we still attempt to stack enough images so that 100ppm photometry is experimentally verified. If so, we can be assured that, in the future, when the system is tweaked to a state with a lower noise floor, which is easily done with the attention of any CCD expert on the TESS team, photometry can only be improved (and dramatically).

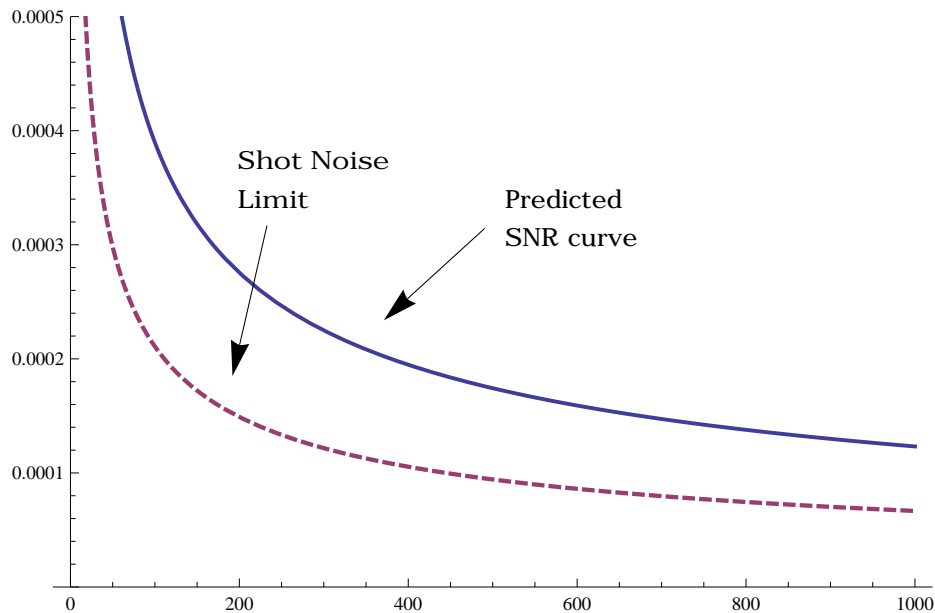


Figure 20: Although the two normalized noise ratios both decrease as  $1/\sqrt{\eta}$ , the two curves asymptote to different values.

We are judicious in our choice of candidate stars. Keeping in mind the effect of the image jitter described in Section 6.3 on the photometry of bright stars, we exclude from our relative photometric analysis the four brightest stars in our field of view: stars 5, 6, 10, and 11 in Figure 15. These are all nearest the light source at the center of the star plate.

In addition, Star 2, the star farthest from the line-of-sight center, is also excluded due to unreliable photometry, the cause of which may be PSF aberration or overall low intensity. The rest of the stars are required to establish a reliable mean intensity curve against which all individual light curves are normalized. Recall that  $M$ , the total number of stars used to calculate the reference mean intensity, should be made as large as possible to limit error. The best statistics, naturally, will be found among the brighter stars.

### 6.4.3 Photometry Results

This section contains reduced data from an overnight session during which 14,000 exposures were taken and summed in groups of 2000 to establish a 7-point light curve for 14 stars. That week, we conducted several of these experimental runs, all with

similar results. What is presented here is the most complete of the bunch, and is representative of the level of photometry we are confident in achieving even operating within the limitations we discussed.

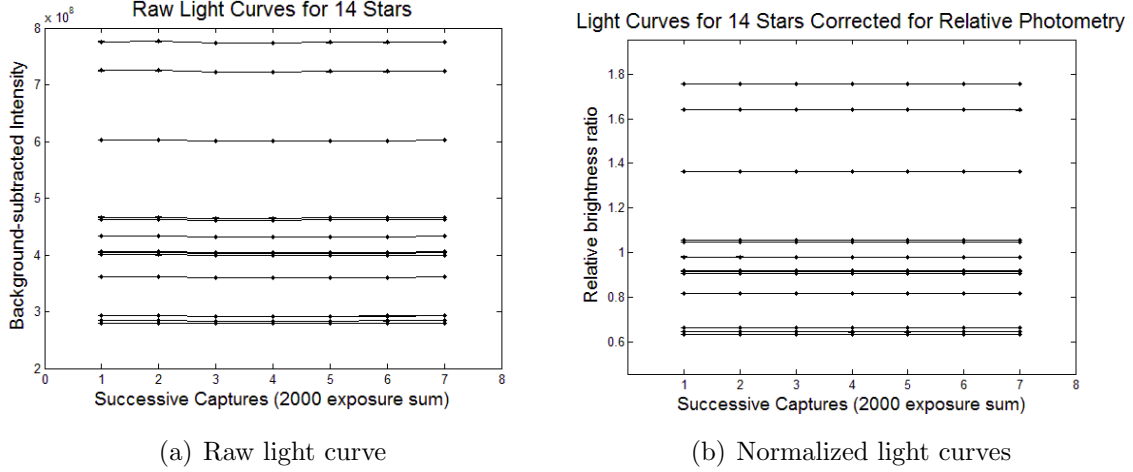


Figure 21: Light curves for 14 stars before and after relative flattening.

Star Number	Relative Intensity	Shot Noise Limit	Theoretical Noise Value	Measured RMS Variation
12	1.75	50	110	$190 \pm 49$
4	1.66	52	115	$149 \pm 39$
15	1.37	57	133	$175 \pm 46$
16	1.06	65	164	$179 \pm 46$
3	1.06	65	164	$285 \pm 74$
14	0.98	67	176	$253 \pm 66$
18	0.92	69	186	$159 \pm 41$
9	0.92	69	186	$331 \pm 86$
1	0.84	73	201	$270 \pm 70$
13	0.83	73	203	$167 \pm 43$
7	0.67	82	246	$360 \pm 94$
19	0.66	82	250	$183 \pm 48$
17	0.65	83	253	$289 \pm 75$
8	0.64	83	257	$399 \pm 104$

Table 1: Photometry achieved by 2000 frame stacks. Average intensity is  $2.25 \times 10^8$  electrons. All noise values are unitless, given in terms of fractional variation in parts per million (ppm).

#### 6.4.4 Analysis

Stacks of 2000 images are used to generate seven-point light curves for the photometry of the brightest stars. Graphical results are displayed in Figure 21. Using a reference value generated by the mean of 14 stars, we are able to achieve sub-200ppm photometry on exactly half (7) of the stars in the frame, while the fractional RMS on an additional 4 hover between 2- and 300 ppm. The mean intensity in units of electrons is  $2.25 \times 10^8$ . See Table 6.4.3 for the more detailed set of results from this test.

In the table, stars are organized in order of relative intensity. Shot noise limit is calculated simply by taking  $1/\sqrt{I_i}$ , where  $I_i$  is the signal in electrons. We do not expect this limit to be reached due to readout noise dominance at the high intensity limit. Equations 26 and 16, combined and reprinted below, are used to calculate the theoretical expected values against which we may compare our photometric results.

$$\sigma_{R_i}/R_i = \sqrt{I_i + 4b^2\eta r^2 \left(1 + \frac{4b^2}{N}\right) + \left(\frac{\sigma_{\bar{I}}}{\bar{I}}\right)^2} \quad (27)$$

The first two terms under the radical count for the shot noise and readout noise in electrons, calculated based on our data collecting and processing techniques while the last term factors in the normalization uncertainty—additional noise that is the result of invoking relative photometry to remove systematic variations across the entire star field. Again, the parameters that correspond to our analysis are  $b = 9$ ,  $\eta = 2000$ ,  $r = 28.4$ , and  $N = 300$ . We’ve changed the designation for readout noise from  $\sigma_R$ , previously, to  $r$  here, to avoid confusion with error on the relative background-subtracted signal.  $I_i = R_i \bar{I}$ , where  $R_i$  is the intensity of any particular star normalized to  $\bar{I}$ , the average intensity of all stars in the frame.

The final column is the measured RMS deviation in the normalized brightness of each of the 14 stars, this is established with a total of 7 data points for each star. The standard deviation formula is shown below for sample-size  $K$  and values  $x_i$ ,

$$s = \sqrt{\frac{1}{K} \sum_i^K (x_i - \bar{x})^2} \quad (28)$$

According to the statistics of the standard deviation distribution [5] [17](Kenny, 1951, and Weisstein, 2009), the variance on the standard deviation can be found via the

rather complicated formula,

$$\sigma_s^2 = \frac{1}{K-1} \left[ K - 1 - \frac{2\Gamma^2\left(\frac{K}{2}\right)}{\Gamma^2\left(\frac{K-1}{2}\right)} \right] s^2 \quad (29)$$

Inserting  $K = 7$ , the equation above reduces to

$$\begin{aligned} \sigma_s^2 &= 0.08s^2 \\ \sigma_s &= 0.28s \end{aligned} \quad (30)$$

We compute the errors on our RMS noise using Equation 30. It is clear that better statistics are possible with an increase in sample size. Unfortunately, because of our stable temperature requirement, we are limited by the capacity of a full nitrogen tank in the number of data points that can be obtained and used to construct the light curve. Data collection was cut off at 14,000 frames when the coolant ran out. However, with lower readout noise and faster readout time, we can hope to achieve better statistics while operating under such an environment. Also on the electronics side, deeper full wells and more useful bits on the A/D converter would allow us to collect more photons per exposure without worry of saturation or nonlinearity. And there is finally, of course, the matter of putting more effort into nitrogen-conserving methods of data taking.

Figure 22 affords us a graphical representation of the content in Table 6.4.3. Given the rough nature of our results, they seem to support well our characterization of the error along the signal path. 9 out of 14, or approximately 2/3 of our data points (stars) have error bars that contain their predicted values, which correlates well with our understanding of the normal distribution. As mentioned before, 7 of 14 stars are seen to exhibit photometry better than 200ppm. However, our results appear to be systematically skewed to a higher noise level than is predicted given the parameters of this investigation. 11 out of 14 stars fall above the theoretical noise curve and 3 fall below. We appear to be slightly underestimating the total noise of the system.

Since it is highly unlikely that we *overestimate* the system noise, this is a rather encouraging sign. Some contributions, from elements such as dark current or pixel-to-pixel sensitivity disparities, were discounted in our calculations but may have played a small role. Our chosen method of temperature control introduced a medium time scale periodic jitter in the position of the stars on the CCD, that, although identifiable, was difficult to quantify without the availability of more stable, comparison data taken with the other previously introduced method of temperature stabilization. Untimely

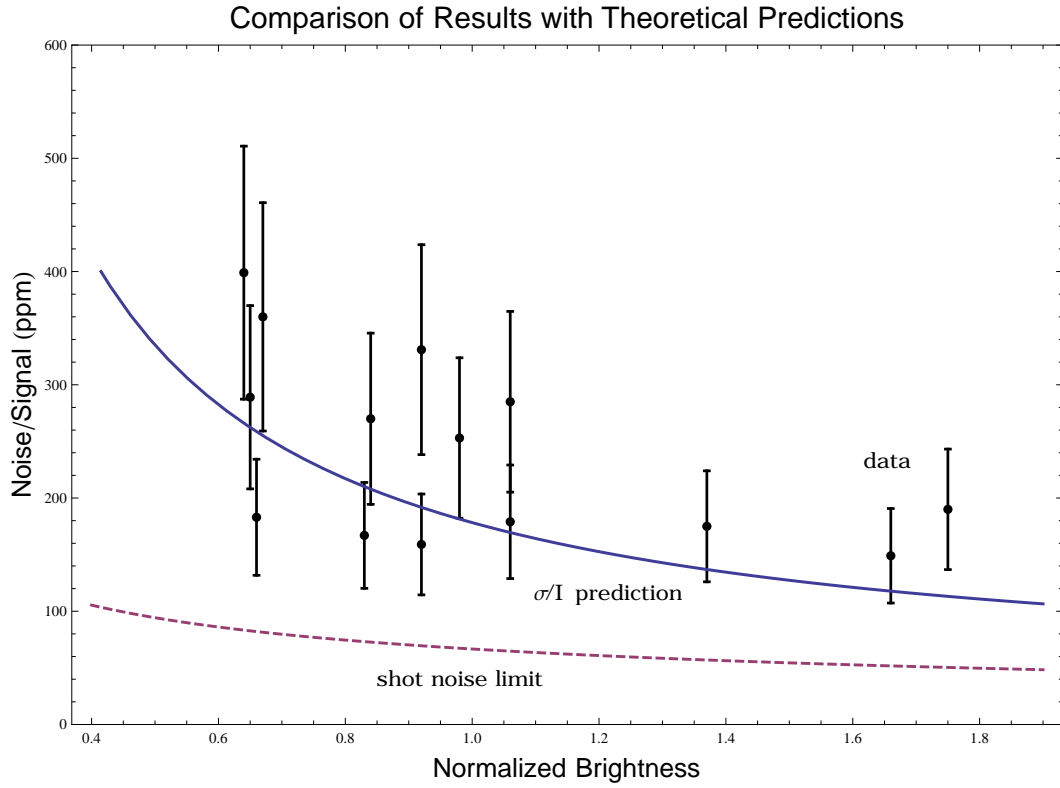


Figure 22: Our results are in good agreement with our predictions based on our understanding of the system and the various factors which contribute to photometric variation. However, we appear to slightly, and systematically, underestimate the total error.



problems with our equipment prevented the acquisition of the latter data set, although this can easily be accomplished when the system recovers its functionality.

## 7 Conclusions and the Future

This document outlined in detail one set of procedures used to conduct photometry tests in the lab. It enumerated the various sources of noise and uncertainty, along with conventional, and sometimes unconventional but necessary, methods of limiting their influence. Along the way, unforeseen issues arose which expanded our knowledge of the CCD-electronics system. Our description and characterization of these unexpected errors may assist in the diagnostic efforts of similar investigations in the future. Additionally, our methods of data reduction are simplistic but even so have proven themselves capable of yielding significant results. As was the case with the gain determination, we remind ourselves that it is not always necessary to use the most complex algorithms at hand in order to achieve the most illuminating results.

Due to a short circuit and subsequent electronics malfunction, we were unable to take further, stable data before the time of this document. But in the few successful runs that we've had, we were able to demonstrate an understanding of the signal path and all major noise components. Our limitations were as follows: 1) time on the equipment which was shared by scientists conducting other tests at MIT and Lincoln Labs, 2) the lack of established hardware and software which resulted in delays during which necessary tools needed to be built or written, and 3) high electronic readout noise of 28 electrons in the same equipment which, in the past, had been demonstrated at levels of 2-3 electrons [3].

The results of our first investigation into TESS hardware photometry are encouraging. We establish sub-200ppm photometry in the laboratory on equipment similar to that which will be used in-flight, using techniques which are repeatable, refinable, and effective. More importantly, we seem to have a good grasp of its contributing components as our data agrees well with our predictions given the constraints we have placed on the system. We identify various anomalies and shortcomings in the instruments which, when tuned, will set the stage for a strong followup investigation. Somewhat inadvertently, we've also demonstrated the stability of photometry in the presence of jitter with magnitude of a fraction of a pixel and a period of several minutes. When the system is back up, the piezo motor should be put into use simulating actual spacecraft jitter obtained from dynamic modeling of its moving parts. Stable

data will be taken with the jitter on and off. We predict this investigation will lead to sub-100ppm results easily. The future of TESS photometry looks bright and busy.

## 8 Acknowledgements

I am grateful for the opportunity to work with an accomplished group of TESS scientists and engineers. A major part of what attracted me to the project in the first place was the collaborative and ambitious spirit of this relatively small community, and I am excited to make whatever contributions I can to its efforts. A special thanks goes out to my thesis advisor, and P.I. of the TESS mission, George Ricker, as well as instrument scientist and my project supervisor Roland Vanderspek, with whom I spent many hours mulling over numbers and figures. Gregory Prigozhin and Steve Kissel from the MIT CCD Laboratory also played in equal parts a significant role in making all parts of this thesis a possibility. Finally, I am grateful to MIT physics graduate student Scott Sanders, who lent me his skills in Adobe Illustrator for the creation of the best of my diagrams, and, of course, to the physics department at this fine institution, for the resources and education that I have been granted.

## References

- [1] Bely, Pierre-Yves. The Design and Construction of Large Optical Telescopes. Springer. pp 57. [2003]
- [2] Bevington, P. R. Data Reduction and Error Analysis for the Physical Sciences. McGraw-Hill. New York. pp. 58-64. [1969]
- [3] Holland, S.E., et al., "A 200 x 200 CCD Image Sensor Fabricated On High-Resistivity Silicon," International Electron Devices Meeting (IEDM) Technical Digest. [1996]
- [4] Howell, Steve B. Handbook of CCD Astronomy. Cambridge University Press. [2000]
- [5] Kenney, J. F. and Keeping, E. S. "The Distribution of the Standard Deviation." Mathematics of Statistics, Pt. 2, 2nd ed. Princeton, NJ: Van Nostrand. [1951]

- [6] Koch, D. G., et al, "CCD photometry tests for a mission to detect Earth-size planets in the extended solar neighborhood". SPIE Conference 4013. [2000]
- [7] Koch, D.; Gould, A. "Differential Photometry." <http://kepler.nasa.gov/sci/basis/diffphot.html> [2005]
- [8] Lundberg, Kent H. [http://web.mit.edu/klund/www/papers/UNP\\_noise.pdf](http://web.mit.edu/klund/www/papers/UNP_noise.pdf). MIT. [2002]
- [9] Mayor, Michael; Queloz, Didier. "A Jupiter-mass companion to a solar-type star." *Nature* 378 (6555): 355359. [1995]
- [10] NIST Standard Reference Database 128. <http://physics.nist.gov/PhysRefData/XrayTrans/index.html>. [2005]
- [11] Nyquist, H. "Thermal Agitation of Electric Charge in Conductors," *Phys. Rev.* 32, 110 [1928]
- [12] Pont, F. et al. "Transiting Extrasolar Planets Workshop," MPA Heidelberg Germany, Sep. 25th-28th, 2006, eds. C. Afonso, D. Wel Drake, & T. Henning. [2007]
- [13] Ricker, G.R, et al. "TESS White Paper". [2007]
- [14] Scholze, F; Rabus,H; Ulm, G. "Measurement of the mean electron-hole pair creation energy in crystalline silicon for photons in the 501500 eV spectral range." *Appl. Phys. Lett.* 69, 2974 [1996].
- [15] Smith, R.; Rahmer, G. "Pixel Area Variations in CCDs and Implications for Precise Photometric Calibration." *IEEE Nuclear Symposium Record*. [2007]
- [16] Conversation with Roland Vanderspek (MIT).
- [17] Weisstein, Eric W. "Standard Deviation Distribution." From MathWorld – A Wolfram Web Resource. <http://mathworld.wolfram.com/StandardDeviationDistribution.html> [2009]